A Study on the Correlation Between Structure and Hole Transport in Semi-Crystalline Regioregular P3HT

ARTICLE *in* ADVANCED ENERGY MATERIALS · FEBRUARY 2013

Impact Factor: 16.15 · DOI: 10.1002/aenm.201200509

3 AUTHORS, INCLUDING:

Volodimyr V. Duzhko
University of Massachusetts Amherst
40 PUBLICATIONS **480** CITATIONS

A Study on the Correlation Between Structure and Hole Transport in Semi-Crystalline Regioregular P3HT

Xiaobo Shen, Volodimyr V. Duzhko, and Thomas P. Russell**

A correlation between the hole transport and corresponding structural properties of the bulk regioregular poly(3-hexylthiophene) (rr-P3HT) is studied as a function of temperature by the time-of-flight (TOF) and wide angle X-ray diffraction (WAXD) techniques. The thermally-reversible structural evolution along the (100) and (020) directions in a semi-crystalline rr-P3HT can be divided into two distinct temperature regions. At T > 120 °C, a large thermal expansion along the π–π stacking direction in the nanocrystals and a deteriorated ordering in the material result in negative slopes of temperature and electric field dependences of hole mobility. The WAXD data suggest that the hole transport is limited by a decrease in the crystallinity and by an increase in the hopping distance along the π–π stacking direction, while the Gaussian Disorder Model (GDM) with temperature-independent parameters cannot be applied. At T < 120 °C, the transport-related structural changes are negligible and the temperature and electric field dependences of hole mobility can be described by the GDM with constant energetic ($\sigma \sim 120$ meV) and positional disorder parameters ($\Sigma \sim 3.33$). These values suggest that the hole transport is limited by the amorphous phase, as commonly seen in disordered polymers. Moreover, a regiorandom P3HT (rra-P3HT), which shows a temperature-independent intermolecular distance of ~15.3Å, provides a route for separate examination of the amorphous phase in rr-P3HT.

1. Introduction

Electronic and optoelectronic applications of polymer-based organic semiconductors, such as organic light-emitting diodes (OLED), organic field-effect transistors (OFET), and organic photovoltaic devices (OPV), are currently approaching the stage of maturing technologies.[1–2] Most of these applications would benefit from the development of new materials with improved charge carrier transport properties and enhanced mobility. Among the numerous potential polymeric semiconductors, a regioregular poly(3-hexylthiophene) has become the prototypical p-type material due to its efficient performance in devices, an ease of processing and a good stability, advancing the commercialization of OPV products (e.g., large area flexible solar panels).[3–5] The initial success has subsequently stimulated a significant amount of synthetic efforts that have led to a widespread material availability in sufficient quantities, development of various structural isomers, like materials with different regioregularities,[4,6,7] and polymers with a wide range of molecular weights.[8–10]

Like all semi-crystalline polymers, rr-P3HT consists of an ordered crystalline phase, with closely packed conjugated chains, and a disordered amorphous phase.[11–13] Due to the nature of rr-P3HT, with a polythiophene backbone and pendant alkyl side-chains, there is also a possibility that rr-P3HT may have a nematic, liquid crystalline-like form, wherein the adjacent chains are oriented with respect to each other but there is no registry between them.[14] The crystalline phase consists of a monoclinic-type unit cells with two chains per cell (a = 1.60 nm, b = 0.78 nm, c = 0.78 nm and γ = 86.5°) as proposed in a recent rotation-tilt electron diffraction study.[15] An amorphous phase, on the other hand, has been modeled by a regiorandom P3HT.[16]

The differences in optical properties of rra-P3HT and rr-P3HT are assigned to a delocalization of electron wave functions along the planarized backbones (intra-chain), i.e., in the (001) direction, and along the π–π stacking (inter-chain), i.e., in the (020) direction, in the latter material.[17,18] Charge transport is more efficient along these directions, as compared to the (100) direction where it is prohibited by the insulating hexyl side chain. The larger mobility in materials with higher regioregularity, as shown with OFET[5] and time-of-flight techniques,[19] emphasizes the role of a high degree of local structural order for improving macroscopic charge transport properties. The preferential alignment of the π–π stacking along the macroscopic charge transport direction imparts an anisotropy into an otherwise random orientation of domains and leads to a further increase in mobility.[20] A recent study by Pingel et al.[21] shows a thermally-activated hole transport with similar activation energies for high molecular weight rr-P3dHT (Mn~27K) on

X. Shen, Prof. T. P. Russell
Department of Polymer Science and Engineering
University of Massachusetts-Amherst
Amherst, MA 01003, USA
E-mail: russell@mail.pse.umass.edu
Dr. V. V. Duzhko
Energy Frontier Research Center "Polymer-based Materials for Harvesting Solar Energy"
University of Massachusetts-Amherst
Amherst, MA 01003, USA
E-mail: duzhko@mail.pse.umass.edu

DOI: 10.1002/aenm.201200509

the local length scale inside the crystalline domains, and on the macroscopic length scale, throughout the semi-crystalline material, measured by the pulse-radiolysis time-resolved microwave conductivity (PR-TRMC) and OFET measurements, respectively. Unlike in the low molecular weight counterpart (7.2 K), a better interconnection between the ordered domains in the high molecular weight rr-P3dHT was argued to be responsible for the enhanced charge transport at high temperatures. On the other hand, the amorphous phase has also been argued to dictate the hole transport in rr-P3HT in several studies.[9,10] In general, it is clear that the hole transport properties in rr-P3HT vary with molecular weight and regioregularity that result in different film morphologies.[4,9,10,21,22] Thus, it would be worthwhile to establish a detailed correlation between the micro- and macroscopic structure in the semi-crystalline rr-P3HT and its hole transport properties, so as to better understand the interplay between the crystalline and amorphous phases.

Using the temperature-resolved TOF and WAXD techniques, we present a detailed investigation of the bulk rr-P3HT with a relatively high molecular weight (Mn~23K) and regioregularity (>98%), and correlate its structural evolution with the macroscopic hole transport at different temperatures. The transport-related structural features in the crystalline and amorphous phases are probed individually, in the regioregular and regiorandom P3HTs, respectively.

2. Results and Discussion

2.1. Hole Transport in rr-P3HT Measured by the TOF Technique

The slow drying of a high-boiling point o-DCB after drop-casting of rr-P3HT solution produces a smooth, thick film. Unlike the spin-coated thin film, whose morphology is far removed from its equilibrium state, the morphology of the slow-dried film is expected to be closer to the thermodynamic equilibrium. The melting of WAXD samples and annealing of TOF samples at high temperatures (as close to the melting point as the sample fabrication procedure permits in order to maintain the geometrical film integrity), was performed for structural properties of samples in the structural and charge transport studies to be similar. Shown in **Figure 1** are the typical photocurrent

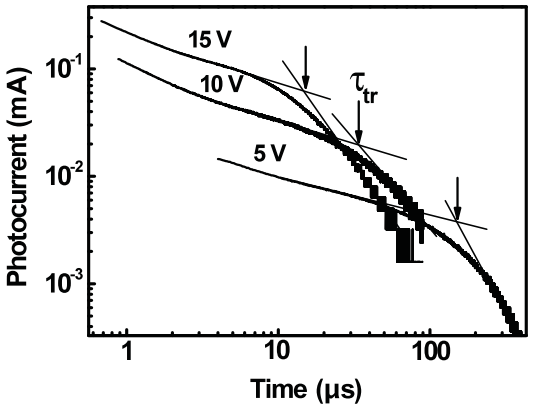

Figure 1. Typical photocurrent transients in rr-P3HT measured at 20 °C for various applied voltages. Transit times are indicated by the black arrows.

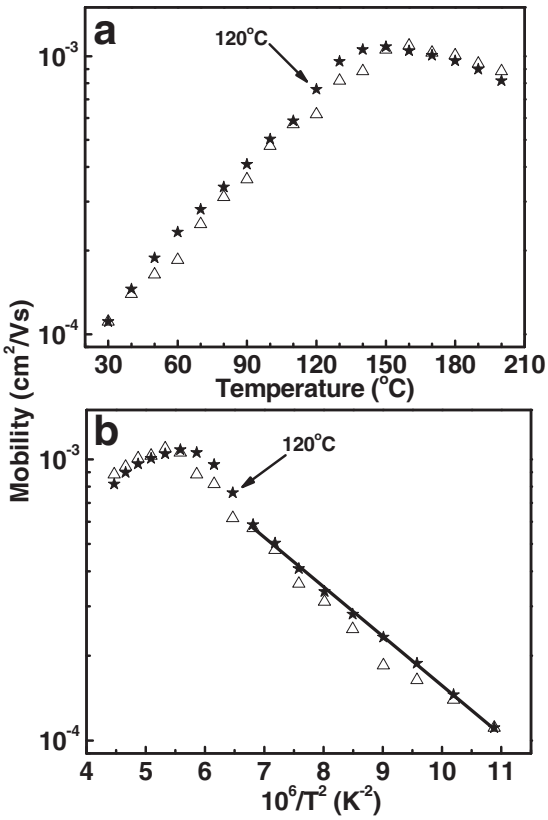

Figure 2. Temperature dependence of hole mobility in rr-P3HT on heating (open triangle) and cooling (solid star): (a) mobility *vs.* T; (b) mobility *vs.* $10^6/T^2$. The black line is the linear fit.

transients measured in rr-P3HT films at 20 °C for different applied voltages. A clear shift of the transit time (τ_{tr}) to smaller values can be seen as the applied voltage increases from 5 V to 15 V, indicating that the passage of holes through the entire thickness of the film is accelerated with the higher electric fields. The hole mobility is determined from $\mu = L^2/(\tau_{tr} \times V)$, where L and V are the film thickness and applied voltage, respectively. The temperature dependences of the hole mobility during the first cooling and second heating cycles are plotted in **Figure 2**. Initially, the hole mobility increases as temperature increases; however, above ~150 °C, the hole mobility begins to decrease, giving rise to a maximum in both the heating and cooling ramps. Moreover, the change of hole mobility, shown on a semi-logarithmic scale in Figure 2b, is linear in $1/T^2$ below 120 °C, as indicated by the linear fit. This behavior has been successfully reproduced on several samples. We note that the temperature-resolved TOF measurements have been previously reported for rr-P3HT,[19,23] however neither a maximum in the mobility nor a negative slope of the temperature dependence have been observed, due to the lower temperature range of those measurements. The Gaussian Disorder Model (GDM),[24] which, on the basis of Monte Carlo simulations, describes the charge carrier hopping in a Gaussian density of states with a Miller-Abrahams-type rate, can be used to analyze the data. Within the framework of this model, an empirical expression

DOI: 10.1002/aenm.201200509

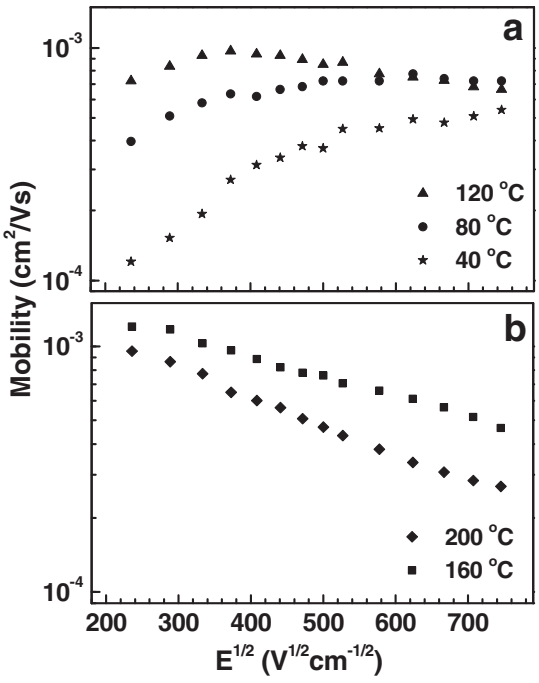

Figure 3. Electric field dependence of hole mobility in rr-P3HT at fixed temperatures: (a) at 40 °C (star), 80 °C (circle) and 120 °C (triangle); (b) at 160 °C (square) and 200 °C (diamond).

for charge carrier mobility (μ) is given by **Equation 1**, where μ_0 is the mobility prefactor, σ/kT is the energetic disorder parameter (width of the density of states) normalized to thermal energy, Σ is the positional disorder parameter, E is the applied electric field, k is the Boltzmann constant and C is an empirical constant.

$$\mu(T, E) = \mu_0 \exp\left[-\left(\frac{2\sigma}{3kT}\right)^2\right] \exp\left\{C\left[\left(\frac{\sigma}{kT}\right)^2 - \Sigma^2\right]\sqrt{E}\right\} \quad (1)$$

According to Equation 1, the logarithmic hole mobility decreases linearly with increasing $1/T^2$ which is in good agreement with the data below 120 °C, shown in Figure 2b. This implies that the increase of hole mobility at lower temperatures is due to a thermal activation of the elementary hopping events. The linearity, however, clearly deviates in the range of high temperatures (above ~120 °C), suggesting a possible structural change with increasing temperature. Also, it is evident that the temperature dependence of hole mobility is reversible on heating and cooling and, therefore, not related to any irreversible structural changes. Furthermore, the electric field dependence of the hole mobility, shown in **Figure 3**, provides more insight into the correlation between hole transport and potential structural changes. For T < 120 °C (40 °C and 80 °C in Figure 3a), the mobility initially increases with increasing electric field, i.e. shows a positive slope in the range of small electric fields, and then levels off; while for T > 120 °C (160 °C and 200 °C in Figure 3b), the mobility shows a continuous, linear decrease over the entire $E^{1/2}$ range, giving rise to a negative slope. Notably, the mobility measured at 200 °C is smaller than that at 160 °C across the same $E^{1/2}$ range, which is consistent with the decrease seen in its temperature dependence. It is interesting to note that the temperature of 120 °C, at which no significant electric field dependence is seen, seems to be the point at which the change of the slope occurs, which is in good agreement with the onset of the deviation observed in the temperature dependence. The GDM was used to understand the sign reversal of the slope in the electric field dependence of mobility. According to Equation 1, the slope is given by the difference between $(\sigma/kT)^2$ and Σ^2 at fixed temperatures. Thus, the relative magnitude of the energetic disorder parameter, a measure of the width of density of states (DOS) normalized to the thermal energy, and the positional disorder parameter, a measure of the inter-site separation and coupling, can be evaluated and related to the difference in the hole mobility over different temperature ranges. In the recent work by Mozer et al.,[25,26] a negative field dependence was also observed, however, for lower temperatures between 250K and 310K. This differs from our electric field dependence results which show a positive dependence up to 120 °C. Although there is no information provided regarding the rr-P3HT employed in their study, this difference might be explained by the differences in the material properties of rr-P3HTs studied, which, in turn, would also result in different energetic and positional disorder parameters. Therefore, the functional dependences of the hole mobility on the temperature and electric field unambiguously suggest the structural changes of rr-P3HT at high temperatures. Consequently, the knowledge of structural changes, namely the changes in crystalline and amorphous phases at different temperatures, is required to fully understand the charge carrier transport properties.

Considering the semi-crystalline nature of rr-P3HT, it is not possible to examine the crystalline and amorphous phases separately. To approach this problem, regiorandom P3HT (rra-P3HT), which is amorphous[19] and chemically identical to rr-P3HT, has been introduced to model the amorphous phase of rr-P3HT.[16]

2.2. Thermal Evolution of the Structure of rr- and rra-P3HTs

The temperature dependence of the d-spacings of (100) and (020) reflections in the rr-P3HT on heating is shown in **Figure 4**. The changes in the peak intensities (I_{max}) and the full widths at half maximum (FWHM) are also shown. As can be seen in Figure 4a, the (100) spacing, characteristic of the distance between the ordered rr-P3HT backbones that are separated by the alkyl side chains, shows a continuous increase with temperature over the entire range from 30 °C to 230 °C. This expansion along the *a* direction was also reported recently in a thin-film geometry.[22,27–29] Considering a resemblance between the hexyl side chain and linear polyethylene (PE), the expansion of rr-P3HT along the *a* direction is somewhat unexpected, since the thermal expansion along the PE backbone is negligible.[30] According to the electron diffraction study by Brinkmann et al.,[15] the hexyl side chains of rr-P3HT are not interdigitated and are tilted with respect to the *a*,*c* plane. A simple comparison between the length of a fully extended *all-trans* hexyl chain and the (100) d-spacing (See Supporting Information) also rules out the possibility of interdigitation, in agreement with previous experimental and theoretical results.[31,32] Based on the

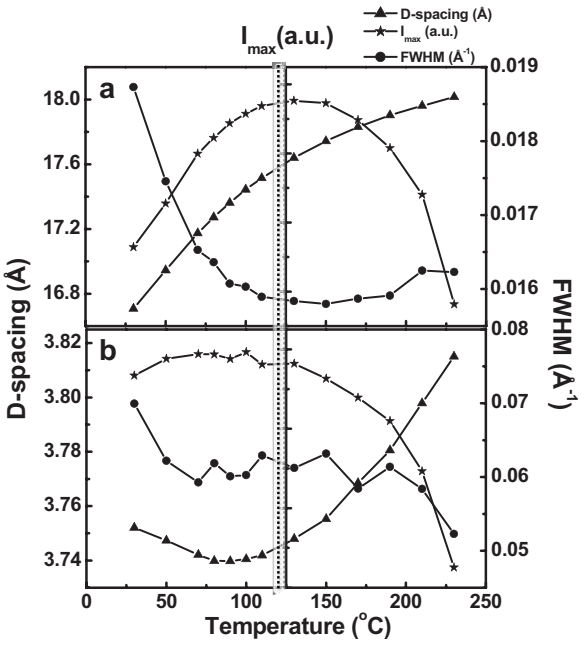

Figure 4. Thermal evolution of d-spacing (triangle), peak full widths at half maximum (FWHM) (circle), peak intensity (I_{max}) (star) of different crystal planes in rr-P3HT during heating: (a) (100) plane; (b) (020) plane. Two distinct regions have been marked by the dotted line.

temperature-resolved infrared spectroscopy measurements by Tashiro et al.,[14] the initial expansion along the *a* direction for T < 120 °C can be associated with the conformational changes of the side chains, the *gauche*$^{\pm}$ conformations in the place of planar *trans* conformation, at higher temperatures.[14,33] The C-C bond rotation would result in a change in the tilting angle of hexyl side chains and, therefore, in an increase in the separation distance between the backbones. A continuous increase of the persistence length along the (100) direction is evidenced by the decreasing FWHM of this reflection from 30 °C to 120 °C, while the overall ordering is improving over the same temperature range, as indicated by the increase in the peak intensity. The persistence length regarding the (100) packing was calculated to be ~35 nm by the Scherrer equation: $L = 0.9\ \lambda/(\beta \times \cos\theta)$, where λ is the wavelength of the incident x-rays, β is the FWHM (2θ), and θ is the Bragg angle. At the temperatures above 120 °C, the persistence length levels off and decreases when approaching the melting point. Meanwhile, the peak intensity starts to plummet, indicating either a reduction in the crystal packing, while the total number of crystals per unit volume remains constant, or that the number of crystals per unit volume has decreased due to a thermal expansion. The change of d-spacing, I_{max} and FWHM in the (020) reflection, characteristic of π–π stacking, is shown in Figure 4b. It is interesting to note that the (020) spacing initially decreases, then levels off from ~70 °C to 110 °C and increases monotonically with increasing temperature prior to melting. Similar to the initial expansion along the (100) direction, the change of tilting angle of hexyl side chain during heating is likely responsible for the initial shrinkage along the π–π stacking direction as well. The persistence length of the crystals along the π–π stacking direction shows an initial increase, then, plateaus near ~70 °C before reaching the melting point. The Scherrer analysis yields a persistence length of ~10 nm along the π–π stacking direction. Finally, the peak intensity, relevant to the ordering and crystallinity in the system, remains relatively constant up to ~130 °C followed by a decrease with increasing temperature as the melting point is approached. This trend is similar to that seen in the (100) direction. On cooling, almost identical d-spacing and similar changes in the FWHM and I_{max} (see Figure S1–S4) were found along both the (100) and (020) directions, indicating a reversibility of the structural change as a function of temperature.

Thus, the structural evolution of rr-P3HT on heating and cooling can be divided into two temperature regions as shown by the dotted line in Figure 4. In Region I, from 30 °C to ~120 °C, there is an initial expansion along the (100) direction (~0.47Å) and a shrinkage along the (020) direction (~0.01 Å), due to a disordering process in the side chain induced by the introduction of the *gauche*$^{\pm}$ conformation. The persistence length and ordering in both directions are increasing. Subsequently, the π–π stacking distance plateaus at ~3.74 Å while the (100) spacing continues to expand (~0.34 Å). Meanwhile, the ordering and persistence of (100) crystal planes continue to increase, whereas, those of the (020) crystal planes remain relatively constant. The degree of crystallinity of the rr-P3HT at 30 °C was determined to be ~59%, suggesting a comparable mass fraction of crystalline and amorphous phases. In Region II above 120 °C, a loss in ordering occurs close to the melting point along both the (100) and (020) directions, resulting in a decrease of crystallinity. A detailed analysis of the degree of crystallinity as a function of temperature will be summarized elsewhere. The linear thermal expansion coefficients along the (100) and (020) directions are determined for T < 120°C: $\alpha_{(100)} = 6.1 \times 10^{-4}\ °C^{-1}$ and $\alpha_{(020)} = -6.6 \times 10^{-5}\ °C^{-1}$ (shrinkage); and for T > 120 °C: $\alpha_{(100)} = 2.2 \times 10^{-4} °C^{-1}$ and $\alpha_{(020)} = 1.8 \times 10^{-4}\ °C^{-1}$. Their similarity at higher temperatures to that of an amorphous PE ($1.7 \sim 2.7 \times 10^{-4}\ °C^{-1}$)[34] indicates a 3-dimensional thermal expansion of disordered hexyl side chain. We suggest that there is a nematic-like liquid crystal phase in Region II, based on the fact that the side chains are in the molten state while the ordered packing of polythiophene backbones is preserved. Notably, larger expansion was observed along both the (100) (~0.5 Å) and (020) (~0.08 Å) directions in comparison to Region I. Interestingly, at ~120 °C, where the Region II in structural data begins, the turning point in TOF data is also seen. The hole transport along the polythiophene backbone, i.e., (001) direction, the fastest propagation pathway, is not expected to change significantly with increasing temperature due to the covalent bonding along the chain. The (100) direction, along the insulating hexyl side chains between the backbones, has limited influence on the hole transport as compared to the more favored π–π stacking direction. Consequently, two mechanisms can be considered to account for the rate-limiting step in the hole mobility above 120 °C: (i) the microscopic π–π stacking expansion inside the crystalline phase which may decrease the hole mobility due to an increase in the hopping distance or (ii) the macroscopic decrease in the crystallinity which would require for holes to pass a greater distance in the amorphous phase. Since the transition between the two regions of distinct structural behavior is rather broad, we took a

DOI: 10.1002/aenm.201200509

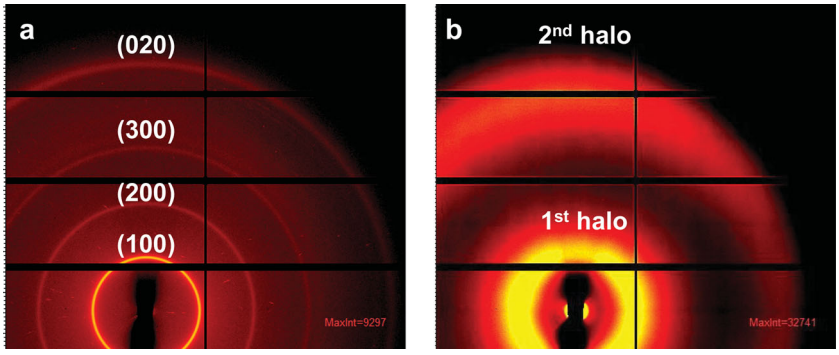

Figure 5. Wide angle X-ray diffraction patterns at 30°C: (a) rr-P3HT; (b) rra-P3HT.

melting point of PE as boundary between them, and relate the structural changes within each region to the respective behavior of hole mobility.

In order to model the amorphous phase in the rr-P3HT, following a previously published approach,[16] we studied the structural properties of rra-P3HT. In contrast to the semi-crystalline rr-P3HT, only two broad halos are seen in the WAXD for rra-P3HT, as shown in **Figure 5**. A very interesting thermal behavior was seen in the temperature dependence of the I(q) *vs.* q profiles, shown in **Figure 6**. From these data, it can be seen that the position of the halo at q~1.45 $Å^{-1}$, corresponding to a spacing of 4.34 Å, shifts to a smaller q with increasing temperature; while the position of the halo at q ~ 0.41 $Å^{-1}$, corresponding to a spacing of 15.3 Å, remains constant as the temperature increases from 30 °C to 250 °C. To understand the difference in the thermal behavior of these two halos, the origins of the halos must be understood. For this purpose, a series of regioregular poly(3-alkylthiophene)s (rr-P3AT) with different alkyl chain lengths were brought above their respective melting points and their diffraction patterns were measured. Two halos were observed for all the molten P3ATs, representing a common amorphous state of P3ATs above T_m. The d-spacings of the halos in each material are tabulated in **Table 1**. Notably, the d-spacings of the second halos are very similar (~4.7 Å), while those of the first halos showed a consistent increase as the length of side chains increase from butyl to decyl. Consequently, the first and second halos have been assigned to the averaged inter- and intra-molecular separation distances, respectively. Schematically shown in **Scheme 1**, the temperature dependent WAXD results of rra-P3HT indicate that the intramolecular distance increases as a result of thermal expansion; however, although the backbones become more twisted and distorted at higher temperatures, the average intermolecular distance between the neighboring backbones remains unchanged. Taking the rra-P3HT as a model of amorphous phase in the rr-P3HT, the constant intermolecular distance in the rra-P3HT implies that the charge hopping distance between the neighboring chains in the amorphous phase of rr-P3HT is independent of temperature.

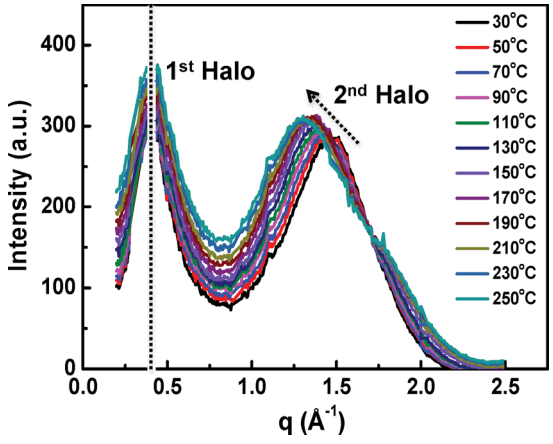

Figure 6. I(q) *vs.* q profiles showing change of two amorphous halos in rra-P3HT during heating.

2.3. Discussion

The picture of hole transport in the bulk rr-P3HT over a broad temperature range can be unveiled from the TOF results, in conjunction with the temperature-resolved WAXD data. Below 120 °C (Region I), the logarithmic hole mobility changes linearly with $1/T^2$, showing a typical thermally-activated hopping which can be described by the GDM. In the corresponding WAXD data, there is no significant change in the d-spacing and crystal persistence length along π–π stacking direction, supporting the applicability of GDM with the temperature-independent energy and positional disorder parameters. From the electric field and temperature dependences of hole mobility below 120 °C, the σ, Σ and C were determined to be 116 meV, 3.3 and 7.9×10^{-4} $(cm/V)^{1/2}$, respectively. An alternate approach is to extract σ from the slope of logarithmic zero field mobility vs. $1/T^2$. The values of Σ and C can be calculated from the slope of electric field dependence ($d\ln\mu/dE^{1/2}$), assuming that σ is constant at lower temperatures. Similar values of $\sigma = 124$ meV, $\Sigma = 3.6$ and $C = 7 \times 10^{-4}$ $(cm/V)^{1/2}$ were obtained. The positional disorder parameter Σ agrees well with value of 3.3 reported by Mozer et al.;[25] however, the energetic disorder parameter σ is somewhat larger than the typical values previously reported for different rr-P3HTs,[19,23,25] suggesting that the difference in the materials might be responsible for this disagreement. Indeed, σ and Σ in our calculations are very similar to the representative values

Table 1. D-spacing comparison of amorphous halos in different P3ATs.

	1st Halo d-spacing/ Å	2nd Halo d-spacing/ Å
rr-P3BT	12.0	4.75
rr-P3HT	15.7	4.76
rr-P3OT	18.5	4.69
rr-P3DT	20.9	4.75
rra-P3HT	15.3	4.80

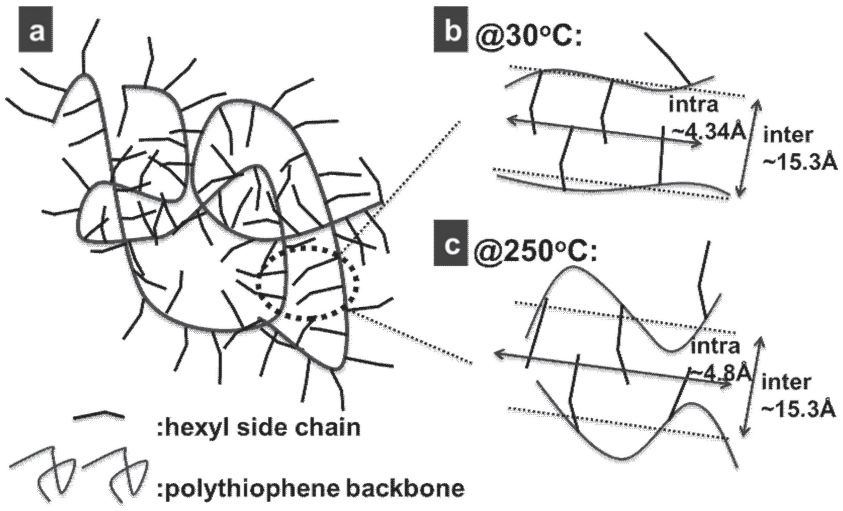

Scheme 1. Molecular structure of rra-P3HT: (a) an overview of two chains; (b) localized view at 30 °C; (c) localized view at 250 °C. The dotted lines in (b) and (c) represent the averaged chain axes. The intermolecular distance is ~15.3 Å, showing an independence of temperature; intramolecular distance increases from ~4.34 Å to ~4.8 Å as a result of thermal expansion.

reported for disordered polymers,[24] implying that the amorphous phase surrounding the crystalline phase, hence, limits the charge carrier transport in Region I. This is also supported by a comparison to the temperature dependence for rr-P3HT obtained from PR-TRMC, which probes the charge transport on a local length scale inside a crystalline domain and, therefore, depends weakly on the molecular weight.[21] The slope derived from the hole mobility vs. $1/T^2$ in PR-TRMC is two orders of magnitude smaller than that from our TOF data in Region I,[21] indicating that the energetic disorder is larger in the case of macroscopic hole transport, which is limited by the amorphous phase in between the crystalline phases.

Above 120 °C (Region II), the increase in the distance between the hopping sites along the π–π stacking direction in the liquid crystal phase and the increase of the amount of amorphous phase occur simultaneously and both can contribute to the decrease in the hole mobility at high temperatures. Assuming that (i) the hole mobility inside the liquid crystal phase remains much larger than in the amorphous phase despite the thermal expansion along the π–π stacking direction and taking into account that (ii) there is no thermal inter-molecular expansion in the amorphous phase, the effect of reduced crystallinity can be further rationalized–the holes travel longer distance in the amorphous phase, resulting in a lower hole mobility. It is interesting to note that the negative slope in temperature and electric field dependences of hole mobility have been recently observed in a discotic liquid crystal mesophase of the triphenylene derivative.[35] Though those data were interpreted in terms of a reduced electron transfer integral due to the thermal activation of phonon modes, they can be described by the thermal expansion along the π–π stacking direction in the columns equally well. This might indicate that the two distinct types of organic materials share the same charge transport mechanism in the respective temperature ranges.

Here, we would like to note that our goal was to characterize the bulk structural and charge transport properties of rr-P3HT and, therefore, the TOF and WAXD techniques with "thick-film" and powder sample geometries, respectively, were selected. Also, the sample fabrication procedures were optimized for the material morphology to be as close to the thermodynamic equilibrium as possible in both cases. A complete thermal reversibility of structural and charge transport data was used as an indication. However, though we think that our choice of experimental techniques and optimized sample preparation conditions has led to that fact that the structural and charge carrier transport properties were compared on the same physical length-scales and in the nearly-identical experimental conditions, the sample geometries and preparation conditions were different.

3. Conclusion

In conclusion, the structural changes of rr-P3HT have been shown to influence the intrinsic hole transport in the bulk rr-P3HT with changing temperature. A separate examination of the amorphous phase in the rr-P3HT is assisted by the introduction of an amorphous rra-P3HT in which a temperature-independent intermolecular distance was observed. For T < 120 °C, no significant hole transport-related structural changes are found and GDM is suitable to describe the hole transport. The temperature and electric field dependences of the hole mobility yield the energetic disorder (σ ~ 120 meV) and the positional disorder (Σ ~ 3.33) parameters, suggesting that the amorphous phase in rr-P3HT limits the hole transport. For T > 120 °C, the GDM with temperature-independent parameters is no longer applicable and both the decreased crystallinity and π–π stacking expansion occur simultaneously, either of which could lead to a decrease in the hole mobility in rr-P3HT at high temperatures. The correlated, temperature-dependent studies of structural properties and charge carrier transport mechanisms facilitate in understanding the material functionality upon its incorporation into electronic and optoelectronic devices. This not only allows gaining a better understanding of the mechanisms of device operation at various temperatures but also serves as an efficient tool for a further optimization of the material properties and device performance.

4. Experimental Section

Materials and Sample Preparation: Regioregular poly(3-hexylthiophene-2,5-diyl) (Mn = 23 k, Mw = 45 k, PDI = 2.0, regioregularity is >98.5%) was provided by Konarka Technologies. Regiorandom poly(3-hexylthiophene-2,5-diyl) (Mw = 72 k, Mn = 22 k, PDI = 3.3, regioregularity is ~57.7%) was purchased from Aldrich (catalog-510823). All the materials were used as received. The regioregularity of each material was calculated from ^{1}H-NMR spectrum based on method described previously.[36] For TOF measurements, samples were prepared by a drop-casting method. A ~30 mg/ml solution of rr-P3HT in ortho-dichlorobenzne (o-DCB) was carefully dropped onto pre-cleaned indium tin oxide

DOI: 10.1002/aenm.201200509

(ITO) coated glass substrate (Thin Film Devices Inc.) on a flat surface inside a N_2-filled glove box. The slow evaporation of o-DCB resulted in a thick film (~1.8 μm) with a smooth surface and uniform thickness. It is noteworthy that the well-controlled drop-cast process with uniform evaporation is important for sample preparation, since gradient structures and surface roughness were usually observed when the evaporation was non-uniform. The sample was kept in a vacuum oven overnight at room temperature to remove the residual solvent. Finally, a semi-transparent Al electrode (25 nm thickness, 6 mm^2 area) was thermally deposited onto the film under high vacuum (2×10^{-6} mbar) using an evaporator in the glove box. After completion of the fabrication, samples were transferred into a HSC302 hot stage and kept in a nitrogen atmosphere at all times. All samples were annealed at 210 °C for 30 minutes in N_2 atmosphere prior to the TOF measurements. The temperature was controlled by an mK1000 temperature controller (INSTEC). For temperature-resolved wide angle X-ray diffraction (WAXD) measurements, a polymer powder was directly melted in a hermetically-sealed differential scanning calorimeter (DSC) pan on a heating stage inside a N_2-filled glove box. Since the pan would be placed vertically in WAXD experiment, a sufficient amount of polymer was placed in the pan so that, during the experiments, the x-ray beam penetrates through the same thickness of sample, even when molten. After cooling to room temperature in the glove box, the pan was rapidly sealed using a crimper. Subsequently, the pan was heated to 250 °C in a DSC (TA instruments, Q200-DSC) and held at that temperature for 10min to remove any thermal history, then ramped down to 150 °C at a rate of 10 °C/min and finally annealed at 150 °C for 30min to induce ordering, prior to the WAXD measurement.

Time-of-Flight (TOF) Measurements: The third harmonic of a pulsed Nd:YAG laser (Continuum Lasers, Surelite II) was used for the photo-excitation of charge carriers at a 355 nm wavelength. Illumination by 4–6 ns pulses through the Al electrode produced a gradient of excess carrier concentration along the smallest film dimension due to a non-uniform light absorption at this wavelength. In order to apply an external bias voltage (V), either a set of electrochemical batteries or a power supply (Stanford Research Systems, PS3100) were used in different voltage ranges. The sign of the applied bias determines if electrons or holes move through the sample. In this study, we report on the transport of holes. The intensity of the laser pulse was kept sufficiently low to avoid a distortion of the electric field, due to a non-uniform distribution of photo-generated charge carriers. A Tektronix TDS 3052C oscilloscope was used to record the photocurrent transients, using a 50 Ω load resistor. A characteristic change of slope in the photocurrent transients indicates the propagation of photo-excited charge carriers through the entire film. An intercept of the two tangent lines to the pre- and post-transit parts of the photocurrent transients in a double-logarithmic scale representation was used to determine the transit time (τ_{tr}).

Wide Angle X-ray Diffraction (WAXD) Measurements: Temperature-resolved WAXD measurements were performed on Beamline 7.3.3 at the Advanced Light Source (ALS) at the Lawrence Berkeley National Laboratory (LBNL). A transmission geometry was used. The wavelength of the x-rays is 1.240 Å and the diffracted photons were collected by a two dimensional Pilatus 1M detector. A heating stage (Linkam) with a built-in sample cell accommodating the DSC sample pan, was mounted into the beamline with a sample-to-detector distance of ~302.6 mm. The sample was heated at a rate of 10 °C/min and then kept at each temperature set-point for 5 min. Each measurement was done with 60s exposure times. During the experiment, a N_2 atmosphere was maintained by purging with N_2. Correction for geometry and polarization was carried out for the diffraction followed by subtraction of background arising from the pan and parasitic scattering.

Supporting Information

Supporting Information is available from the Wiley Online Library or from the author.

Acknowledgements

This material is based upon work supported as part of Polymer-Based Materials for Harvesting Solar Energy, an Energy Frontier Research Center funded by the U.S. Department of Energy, Office of Science, Office of Basic Energy Sciences under contract DE-SC0001087 and by (TPR) the U.S. Department of Energy Office of Basic Energy Science under contract DEFG02-96ER45612.

Received: July 10, 2012
Published online:

[1] G. Dennler, M. C. Scharber, C. J. Brabec, *Adv. Mater.* **2009**, *21*, 1323.
[2] C. J. Brabec, N. S. Sariciftci, J. C. Hummelen, *Adv. Funct. Mater.* **2001**, *11*, 15.
[3] M. T. Dang, L. Hirsch, G. Wantz, *Adv. Mater.* **2011**, *23*, 3597.
[4] C. H. Woo, B. C. Thompson, B. J. Kim, M. F. Toney, J. M. J. Fréchet, *J. Am. Chem. Soc.* **2008**, *130*, 16324.
[5] H. Sirringhaus, N. Tessler, R. H. Friend, *Science* **1998**, *280*, 1741.
[6] Y. Kim, S. Cook, S. M. Tuladhar, S. A. Choulis, J. Nelson, J. R. Durrant, D. D. C. Bradley, M. Giles, I. McCulloch, C.-S. Ha, M. Ree, *Nat. Mater.* **2006**, *5*, 197.
[7] D. P. McMahon, D. L. Cheung, L. Goris, J. Dacuña, A. Salleo, A. Troisi, *J. Phys. Chem. C* **2011**, *115*, 19386.
[8] R. J. Kline, M. D. McGehee, E. N. Kadnikova, J. Liu, J. M. J. Fréchet, *Adv. Mater.* **2003**, *15*, 1519.
[9] A. Zen, M. Saphiannikova, D. Neher, J. Grenzer, S. Grigorian, U. Pietsch, U. Asawapirom, S. Janietz, U. Scherf, I. Lieberwirth, G. Wegner, *Macromolecules* **2006**, *39*, 2162.
[10] R. J. Kline, M. D. McGehee, E. N. Kadnikova, J. Liu, J. M. J. Fréchet, M. F. Toney, *Macromolecules* **2005**, *38*, 3312.
[11] D. Chen, A. Nakahara, D. Wei, D. Nordlund, T. P. Russell, *Nano Lett.* **2010**, *11*, 561.
[12] D. Chen, F. Liu, C. Wang, A. Nakahara, T. P. Russell, *Nano Lett.* **2011**, *11*, 2071.
[13] M. Brinkmann, P. Rannou, *Adv. Funct. Mater.* **2007**, *17*, 101.
[14] K. Tashiro, K. Ono, Y. Minagawa, M. Kobayashi, T. Kawai, K. Yoshino, *J. Polym. Sci., Part B: Polym. Phys.* **1991**, *29*, 1223.
[15] N. Kayunkid, S. Uttiya, M. Brinkmann, *Macromolecules* **2010**, *43*, 4961.
[16] K. Vakhshouri, D. R. Kozub, C. Wang, A. Salleo, E. D. Gomez, *Phys. Rev. Lett.* **2012**, *108*, 026601.
[17] X. M. Jiang, R. Österbacka, O. Korovyanko, C. P. An, B. Horovitz, R. A. J. Janssen, Z. V. Vardeny, *Adv. Funct. Mater.* **2002**, *12*, 587.
[18] J. Clark, C. Silva, R. H. Friend, F. C. Spano, *Phys. Rev. Lett.* **2007**, *98*, 206406.
[19] R. Mauer, M. Kastler, F. Laquai, *Adv. Funct. Mater.* **2010**, *20*, 2085.
[20] H. Sirringhaus, P. J. Brown, R. H. Friend, M. M. Nielsen, K. Bechgaard, B. M. W. Langeveld-Voss, A. J. H. Spiering, R. A. J. Janssen, E. W. Meijer, P. Herwig, D. M. de Leeuw, *Nature* **1999**, *401*, 685.
[21] P. Pingel, A. Zen, R. D. Abellón, F. C. Grozema, L. D. A. Siebbeles, D. Neher, *Adv. Funct. Mater.* **2010**, *20*, 2286.
[22] S. Joshi, P. Pingel, S. Grigorian, T. Panzner, U. Pietsch, D. Neher, M. Forster, U. Scherf, *Macromolecules* **2009**, *42*, 4651.
[23] A. M. Ballantyne, L. Chen, J. Dane, T. Hammant, F. M. Braun, M. Heeney, W. Duffy, I. McCulloch, D. D. C. Bradley, J. Nelson, *Adv. Funct. Mater.* **2008**, *18*, 2373.
[24] H. Bässler, *Phys. Status Solidi B* **1993**, *175*, 15.
[25] A. J. Mozer, N. S. Sariciftci, *Chem. Phys. Lett.* **2004**, *389*, 438.
[26] A. J. Mozer, N. S. Sariciftci, A. Pivrikas, R. Österbacka, G. Juška, L. Brassat, H. Bässler, *Phys. Rev. B* **2005**, *71*, 035214.
[27] S. Lilliu, T. Agostinelli, E. Pires, M. Hampton, J. Nelson, J. E. Macdonald, *Macromolecules* **2011**, *44*, 2725.

[28] E. Verploegen, R. Mondal, C. J. Bettinger, S. Sok, M. F. Toney, Z. Bao, *Adv. Funct. Mater.* **2010**, *20*, 3519.
[29] T. Agostinelli, S. Lilliu, J. G. Labram, M. Campoy-Quiles, M. Hampton, E. Pires, J. Rawle, O. Bikondoa, D. D. C. Bradley, T. D. Anthopoulos, J. Nelson, J. E. Macdonald, *Adv. Funct. Mater.* **2011**, *21*, 1701.
[30] P. R. Swan, *J. Polym. Sci.* **1962**, *56*, 403.
[31] R. J. Kline, D. M. DeLongchamp, D. A. Fischer, E. K. Lin, L. J. Richter, M. L. Chabinyc, M. F. Toney, M. Heeney, I. McCulloch, *Macromolecules* **2007**, *40*, 7960.
[32] R. Colle, G. Grosso, A. Ronzani, C. M. Zicovich-Wilson, *Phys. Status Solidi B* **2011**, *248*, 1360.
[33] P. J. Flory, *Statistical Mechanics of Chain Molecules*, Interscience Publishers, New York, USA **1969**.
[34] F. C. Stehling, L. Mandelkern, *Macromolecules* **1970**, *3*, 242.
[35] V. Duzhko, A. Semyonov, R. J. Twieg, K. D. Singer, *Phys. Rev. B* **2006**, *73*, 064201.
[36] T.-A. Chen, X. Wu, R. D. Rieke, *J. Am. Chem. Soc.* **1995**, *117*, 233.

Adv. Energy Mater. **2012**,
DOI: 10.1002/aenm.201200509